

A Study on Microstructure and Phase Transformation in the Weld Fusion Zone of TIG-Welded IN939 with IN625 and IN718 as Filler Metal



H. KAZEMPOUR-LIASI, M. TAJALLY, and H. ABDOLLAH-POUR

Microstructure and phase transformations were investigated in the weld fusion zone (WFZ) of tungsten inert gas (TIG)-welded IN939 nickel-based superalloy with IN718 and IN625 alloys used as filler metal. The optical and field-emission scanning electron microscopy (FESEM) and also energy dispersive spectroscopy (EDS) were utilized for the microstructural study of the WFZ. The microstructural examination showed that the Nb and Ti elements were microsegregated in the inter-dendrite region, causing a significant concentration gradient between the core and the inter-dendrite region within the WFZ. Observations indicated the formation of the (Nb, Ti) C carbide phases in the solidification process. With a thickness of about $0.2 \mu\text{m}$, some plate-like δ phase was observed in the WFZ of both samples upon heat treatment at 750°C . The results of X-ray diffraction analysis (XRD) confirmed the presence of the δ phase in the WFZ. However, the δ phase disappeared at temperatures beyond 1000°C . The occurrence of phase transformation during the solidification process was identified by differential thermal analysis (DTA). The WFZ was seen to solidify in the temperature range of 1370°C to 1270°C .

<https://doi.org/10.1007/s11661-020-05690-8>

© The Minerals, Metals & Materials Society and ASM International 2020

I. INTRODUCTION

NI-BASED alloys represent an important class of engineering materials and have been used in various environments and applications. Among others, examples of the application of these alloys in the energy industry include those in hot gas path components, stationary and rotary gas turbine blades, gas turbine combustion chambers, *etc.* Fusion welding is a technique for manufacturing and repairing such components.^[1,2] As a casting nickel-based superalloy, IN939 is precipitation-hardened upon precipitation of the γ' phase. It was originally designed for long life and excellent corrosion resistance at elevated temperatures (up to 800°C), making it a material of choice for stationary and rotary blades of gas turbines.^[3,4] Superalloy welding with some filler metal of different chemical composition alters the chemical composition of the weld fusion zone (WFZ) depending on the dilution level. This leads to the formation of various phases in the WFZ

upon the solidification or post-weld heat treatments (PWHT).

In superalloy welding, the microstructure of the weld controls the properties and reliability of the weldments; it can be greatly enhanced by the segregation and phase transformations occurring during the solidification stage.^[5] Microsegregation of the alloying elements during the solidification of the fusion zone tends to release liquid elements in the inter-dendrite regions, leading to the formation of secondary phases in these regions in the terminal stages of solidification. Some of the important reinforcement elements (*e.g.*, B, Zr) may be tied up to these particles.^[5-7] A Ni-based alloy consists of a matrix phase and some secondary phase(s). The most frequently used secondary phases for Ni- and Fe-Ni-bases superalloys include MC, $M_{23}C_6$, M_6C , and M_7C_3 carbides, γ' -Ni₃(Al, Ti), γ'' -Ni₃Nb, η -Ni₃Ti, and δ -Ni₃Nb intermetallic compounds.^[8] The γ'' -reinforced superalloys are susceptible to the formation of a δ phase upon over aging. The δ phase is a stable form of the Ni₃Nb with an orthorhombic (D0_a) crystal structure.^[9] An increase in the concentration of Nb contributes to the formation of the δ phase.^[10] Formed in the temperature range of 650°C to 980°C , this phase has its characteristics heavily dependent on the formation temperature. Given that the formation of the δ phase in large amounts results in severe degradation of material properties, measures must be taken to avoid it.^[2]

M. TAJALLY and H. ABDOLLAH-POUR are with the Faculty of Materials and Metallurgical Engineering, Semnan University, Semnan, Iran. Contact e-mail: m_tajally@semnan.ac.ir. H. KAZEMPOUR-LIASI is with the Faculty of Materials and Metallurgical Engineering, Semnan University and also with the Metallurgy Department, Niroo Research Institute, Tehran 14686, Iran.

Manuscript submitted November 9, 2019.

Article published online March 2, 2020

The formation of the δ phase has been reported in the IN625 and IN718 alloys.^[9–15] However, no data have been reported on the formation of this phase and related phase transformations in the WFZ of the IN939 superalloy welded using IN625 and IN718 as filler metal. The present work presents a study on the microstructural characteristics and phase transformations in the WFZ of TIG-welded IN939 with IN625 and IN718 as filler metal.

II. MATERIALS AND METHODS

Coupons with dimensions of $2 \times 4 \times 8$ cm and $1 \times 10 \times 20$ were cut from IN939-made gas turbine blades using a wire electrical discharge machine (WEDM). Table I shows the chemical composition of the IN939 superalloy and the filler metals used in this study. The coupons were then subjected to pre-weld heat treatments: annealing at 1160 °C for 4 hours and then cooling to 920 °C at 2 °C/min followed by air-cooling (according to a recent development by the authors^[16]). The pre-weld heat-treated coupons were then TIG-welded manually using a 10-V DC current at 60 A and wires of each filler metal with a diameter of 1.2 mm.

Transversely to the welding direction, seven sections of each weldment (Figure 1(a)) were cut and prepared for metallographic examinations by polishing and etching. The etching was done *via* two approaches: (1) etching in a solution containing 0.3 g of MoO₃, 10 mL of HNO₃, 10 mL of HCl, and 15 mL of H₂O, and (2) electro-etching in a solution containing 12 mL of H₃PO₄, 40 mL of HNO₃, and 48 mL of H₂SO₄ using a 6-V DC current for about 5 seconds. The specimens had their microstructures investigated using optical and field-emission scanning electron microscopy (FESEM) together with an energy dispersive spectroscopy (EDS) probe. Cross-sections of the specimens were investigated in two states: (1) as-welded and (2) post-weld heat-treated. In this study, the PWHT was applied under two scenarios, namely an industry-standard scenario and a special scenario considered in this study (Table II). Prior to the microstructural studies, the samples were ground to a particle size of 0.5 mm to remove possible oxidated layers (Figure 1(b)).

The X-ray diffraction (XRD) studies were used to identify the phases by using a Siemens D500 diffractometer operating in continuous scanning mode. The apparatus radiated Cu K₁ ($\lambda = 0.154056$ nm) at different values of 2θ in the range of 4 to 120 deg at a step size of 0.02 deg and a time step of 20 seconds. In order to determine the mechanical properties of the weldments, tensile tests were carried out according to ASTM-E8 and ASTM-E21 at a strain rate of 0.16 mm/min until the yield point and then 1.6 mm/min. For this purpose, sheets of 2 mm thickness were cut from the surface of the blocks using a wire electrical discharge machine (WEDM). Tensile specimens were then prepared from the sheets with dimensions according to Figure 1(c). The depth of the filled section in tensile specimens was equal to the thickness of the samples.

The differential thermal analysis (DTA) was performed on a Bahr STA 504 instrument. Weighed to ≈ 0.5 g, the specimens were thermally cycled from room temperature to 1440 °C at a heating rate of 5 °C/min under a flow of argon.

The JMatPro Software was utilized in conjunction with the Ni-DATA database to predict the existing phases and phase transformations in the WFZ.

III. RESULTS AND DISCUSSION

A. Microstructural Investigation of the WFZ upon Standard PWHT

Figure 2 shows the images of the weld region in the as-welded state. According to the figure, no trace of solidification cracking in the WFZ was observed while the dendritic structure of the weld region is visible. The γ' solvus temperature is in the range of 1080 °C to 1100 °C,^[17] so it is expected that in pre-weld heat-treated samples, these phase will be completely dissolved and a new microstructure formed with less susceptibility for weld cracking.^[16]

During the solidification process, grains tend to grow in a direction perpendicular to the weld pool boundary as it delineates the direction of the maximum temperature gradient and hence maximum heat extraction, while columnar dendrites or cells within each grain tend to grow in the easy-growth direction.^[17] The dendrite spacing on the secondary arm (λ_S) was about 4 μ m. From the dendrite spacing, one can calculate the cooling rate via the following equation^[5,18]:

$$\lambda_S = K_S \phi^n \quad [1]$$

where ϕ is the cooling rate and K_S and n are constants. Using the values of $K_S = 4.7 \times 10^{-2}$ mm $k^{1/3}$ s^{-1/3}, $\lambda_S = 4$ μ m and $n = -0.4$,^[5] the cooling rate in the WFZ is about 480 °C/s, which is very high compared to those experienced in the investment casting (~ 5 °C/s). The cooling rate of about 550 °C/s has already been reported for the solidification of the IN738 fusion zone.^[5]

Segregation of the alloying elements in the WFZ was observed as black points in Figure 2. These were formed in the inter-dendrite region during the final stages of the solidification process. The level of segregation of the alloying elements in the as-welded structures can be expressed as the partition coefficient between the inter-dendrite region and the dendrite core: $K = C_D/C_I$, where C_I and C_D are the concentrations of the element in the inter-dendrite region and the dendrite core, respectively.^[19,20]

Figure 3 shows an image of the WFZ upon the PWHT. The specimen welded with IN625 as filler metal. As seen, upon the PWHT (for both 3- and 4-step PWHT cycles), a number of plate-like and needle-shaped phases appeared in the microstructure. These phases were observed both inside the grains (Figures 3(b) through (d)) and along the grain boundaries (Figure 3(a)). This suggests that these phases are rich in the elements segregated at the end of the solidification process of the

Table I. Chemical Compositions of the IN939, IN625, and IN718 Alloys Used in This Work (Wt Pct)

Alloy		Al	Ti	W	Ta	Cr	C	Fe	Nb	Si	Zr	Co	Mo	Ni	Refs.
IN939	base metal	2.0	3.7	2.2	1.4	22.5	0.15	0.5	1.1	0.2	0.14	19	—	bal.	3
IN625	filler metal	0.2	0.2	—	—	21.5	0.05	2.5	3.6	—	—	—	9	bal.	18
IN718		0.52	1.0	—	—	18.5	0.03	18.04	5.3	—	—	0.13	3.04	bal.	18

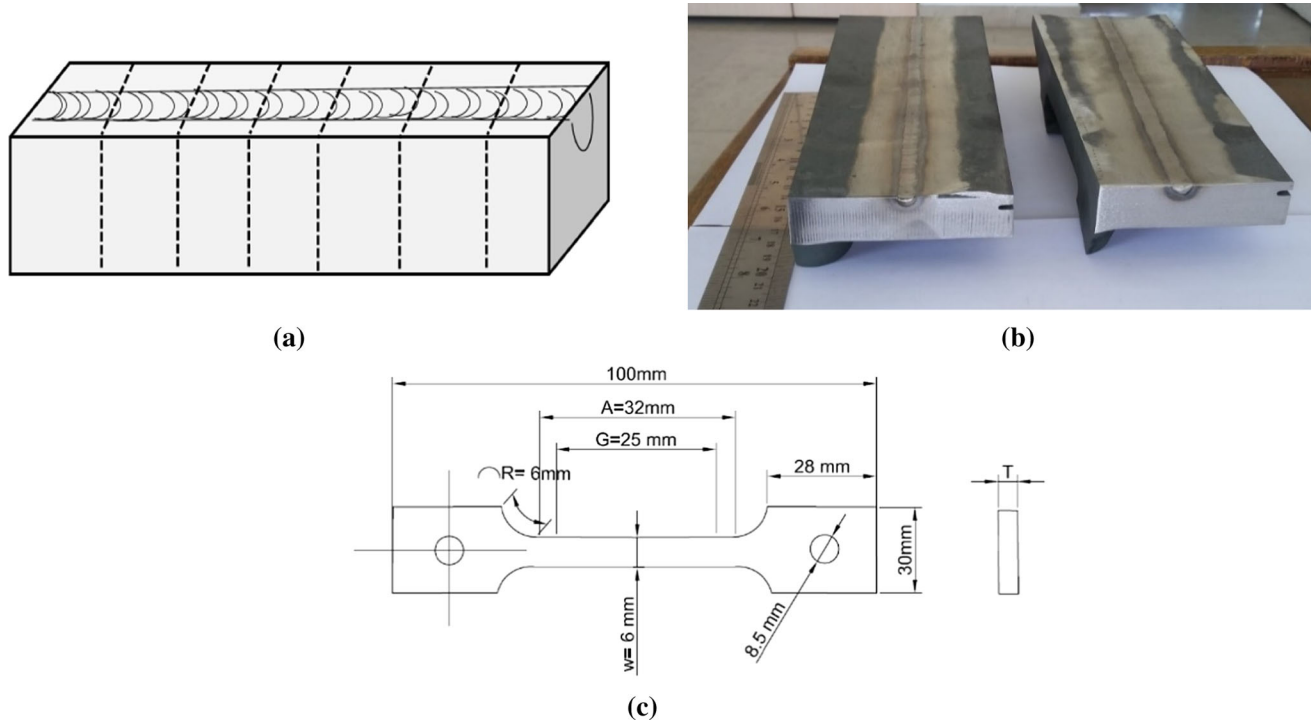


Fig. 1—Bead-welded coupons prepared for this study. (a) Schematic view of coupons for metallographic examinations. (b) Coupons in order to determine the mechanical properties of the weldments. (c) Dimensions of tensile specimens.

Table II. The PWHT Cycles Applied for This Study

Heat Treatments	Type of Operation
1160 °C/4 h/AC + 845 °C/16 h/AC	2 Step (Standard)
1160 °C/4 h/AC + 1000 °C/6 h/AC + 800 °C/6 h/AC	3 Step (Standard)
1160 °C/4 h/AC + 1000 °C/6 h/AC + 900 °C/24 h/AC + 700 °C/16 h/AC	4 Step (Standard)
700 °C/8 h/AC	1 Step
750 °C/8 h/AC	1 Step
850 °C/8 h/AC	1 Step
950 °C/8 h/AC	1 Step
1000 °C/8 h/AC	1 Step
1293 °C/WQ	1 Step
1315 °C/WQ	1 Step
1350 °C/WQ	1 Step

AC, Air-cooled; WQ, Water-quenched.

WFZ. As can be seen, the above heat treatments cycles have not been sufficient to diffusion of segregated elements from the inter-dendritic region. After these processes, plate-like and needle-shaped phases are

formed in the inter-dendritic region. The temperature conditions of the formation of these phases and their corresponding transformation will be described in the following sections.

Figures 4 and 5 show SEM images of the WFZ in the specimens welded with IN625 as filler metal upon 3-step and 4-step PWHTs, respectively. The plate-like and needle-shaped phases and particles with dimensions of less than 100 nm are visible in these images. Given the higher temperature and longer time of the aging process in the 2-step (845 °C/16 h) and 4-step cycles (900 °C/24 h), rather than the 3-step cycle (800 °C/6 h), the needle-shaped particles had larger potentials for growth into plate-like grains. A previous work has reported the effect of temperature on the morphology of the IN625 weld particles.^[21,22]

According to Figure 4, these phases were precipitated along the grain boundaries and gaps were observed around the needle-shaped particles (Figure 4(b)). The intersecting pattern of precipitation and growth of these precipitants is shown in Figure 5(b). Other researchers have reported the intersecting network of δ particles in the IN718 weld zone.^[23] The nucleation and growth of

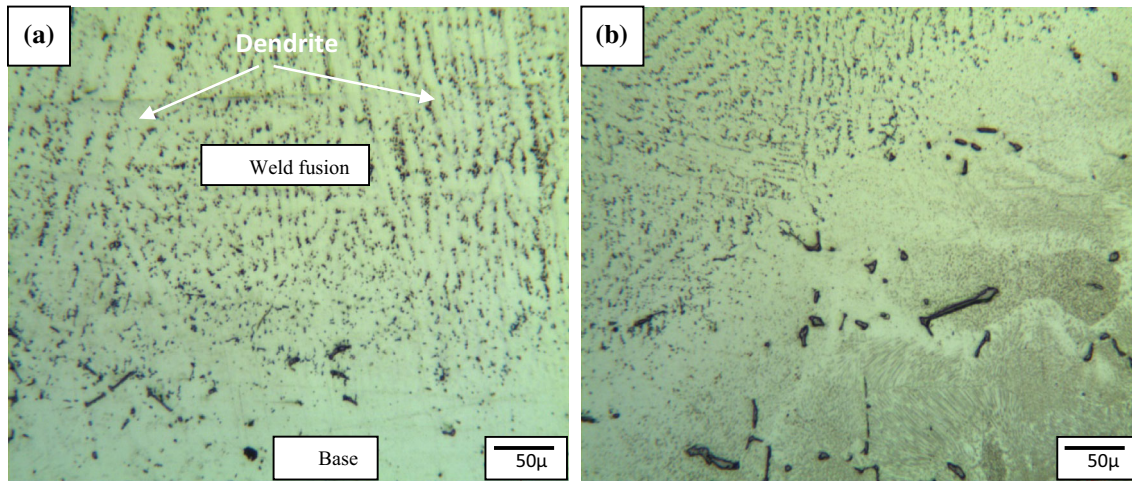


Fig. 2—Optical micrographs showing the dendritic microstructure of the as-welded WFZ with (a) IN625 and (b) IN718 as filler metal.

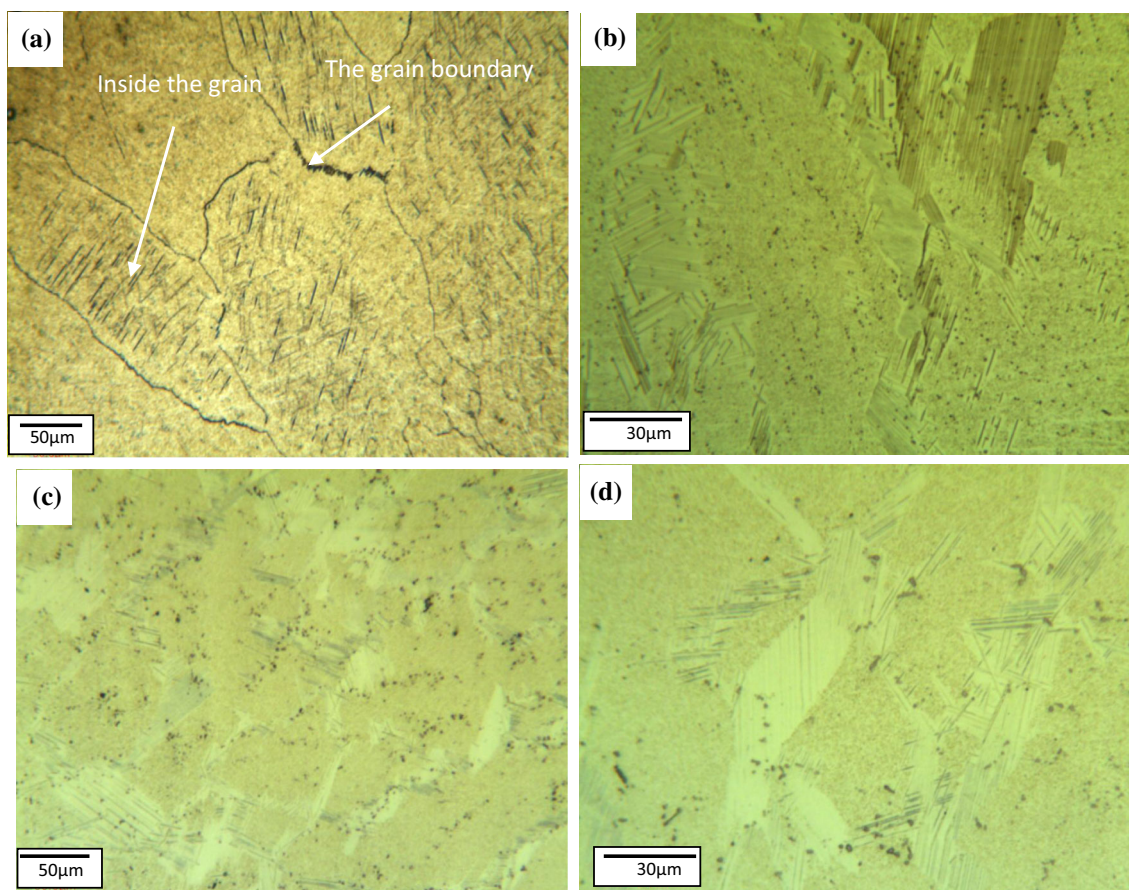


Fig. 3—Optical micrographs showing plate-like and needle-shaped phases in the WFZ on the specimen welded with IN625 as filler metal and then subjected to the (a) 2-step, (b) 3-step, (c) and (d) 4-step PWHT cycles.

the δ phase on the conjugate plane of the γ'' phase lead to the formation of an intersecting network.^[22,23]

Results of the EDS analysis on the plate-like particles are presented in Table III, indicating significant amounts of Nb. Given the morphology and the result

of the EDS analysis, these particles represent the δ phase (δ -Ni₃Nb). The superalloy that is precipitation-reinforced with γ'' -Ni₃Nb phase is susceptible to the δ phase formation during the processing or operating stages. The presence of this phase has been reported in

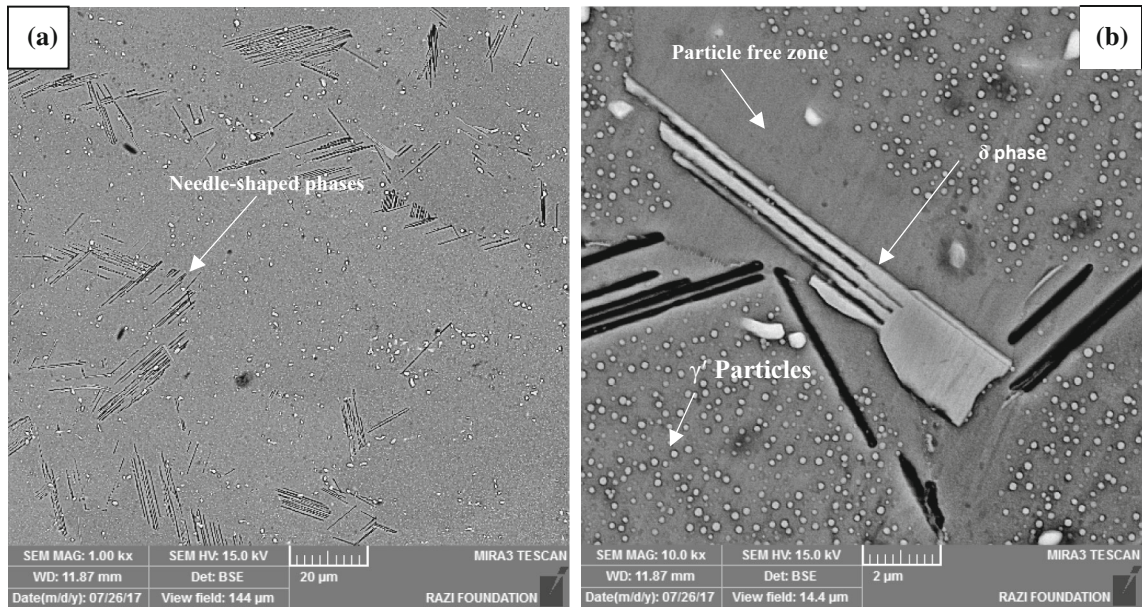


Fig. 4—FESEM micrographs of the WFZ of the specimen welded with IN625 as filler metal, subjected to the 3-step PWHT cycle, indicating (a) the needle-shaped phases and (b) the precipitation of the δ and γ' particles and formation of the PFZ around the δ phase.

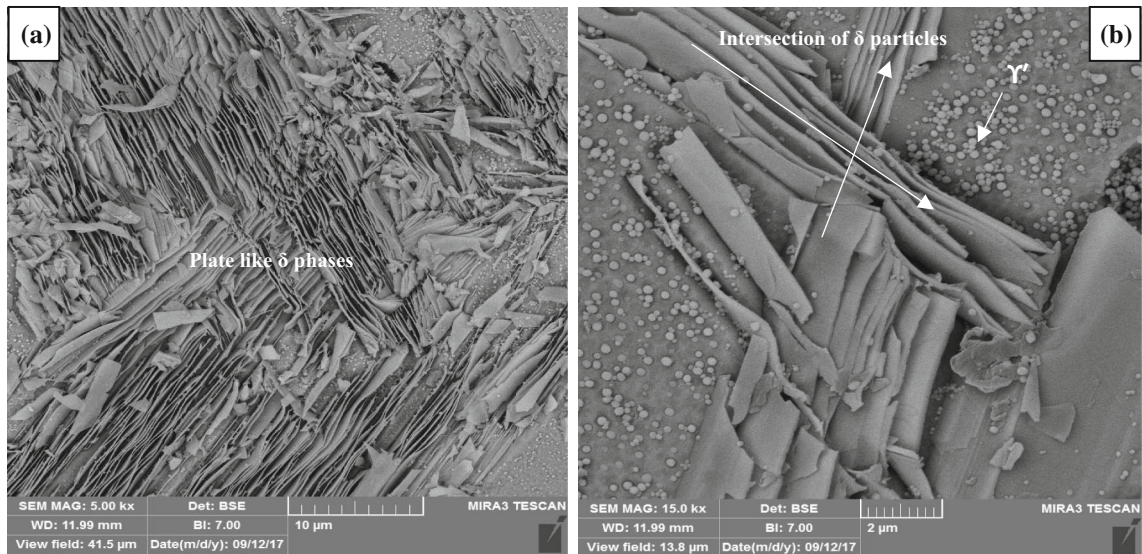


Fig. 5—FESEM micrographs of the WFZ of the specimen welded with IN625 as filler metal, subjected to the 4-step PWHT cycle, indicating (a) the plate-like δ phases and (b) the precipitation of the δ and γ' particles and the intersecting pattern of δ particle.

Table III. Quantitative Analysis of the Composition of the Plate-Like Particles (Fig. 5) Using the EDS Data

Element	Al	Ti	Cr	Co	Nb	Mo	Ta	Ni
Wt Pct	8.74	12.85	4.54	1.95	31.91	4.40	0.40	bal.
At. Pct	19.00	15.74	5.12	1.95	20.16	2.69	0.13	bal.

Nb-containing alloys, *e.g.*, IN625 and IN718, under various conditions.^[2,9]

Figure 6 shows SEM images of the WFZ in the specimens welded with IN625 and IN718 as filler metals

upon 3-step PWHTs. According to Figure 6, in addition to the needle-shaped phases, white particles of approximately 1 μm size can also be seen in the microstructure. These particles were observed in both specimens. Results of the EDS analysis on the white particle were presented in Figure 6(d). According to the results, these carbides are MC-Carbides ($M = \text{Ti, Nb, and Ta}$).

Figure 7 shows the image of the WFZ of the specimen welded with IN718 as filler metal, indicating the presence of plate-like and circular particles in the microstructure of this specimen. The thickness of the plate-like phase in this specimen was about 0.2 μm . Table IV tabulates the results of the EDS analysis on the

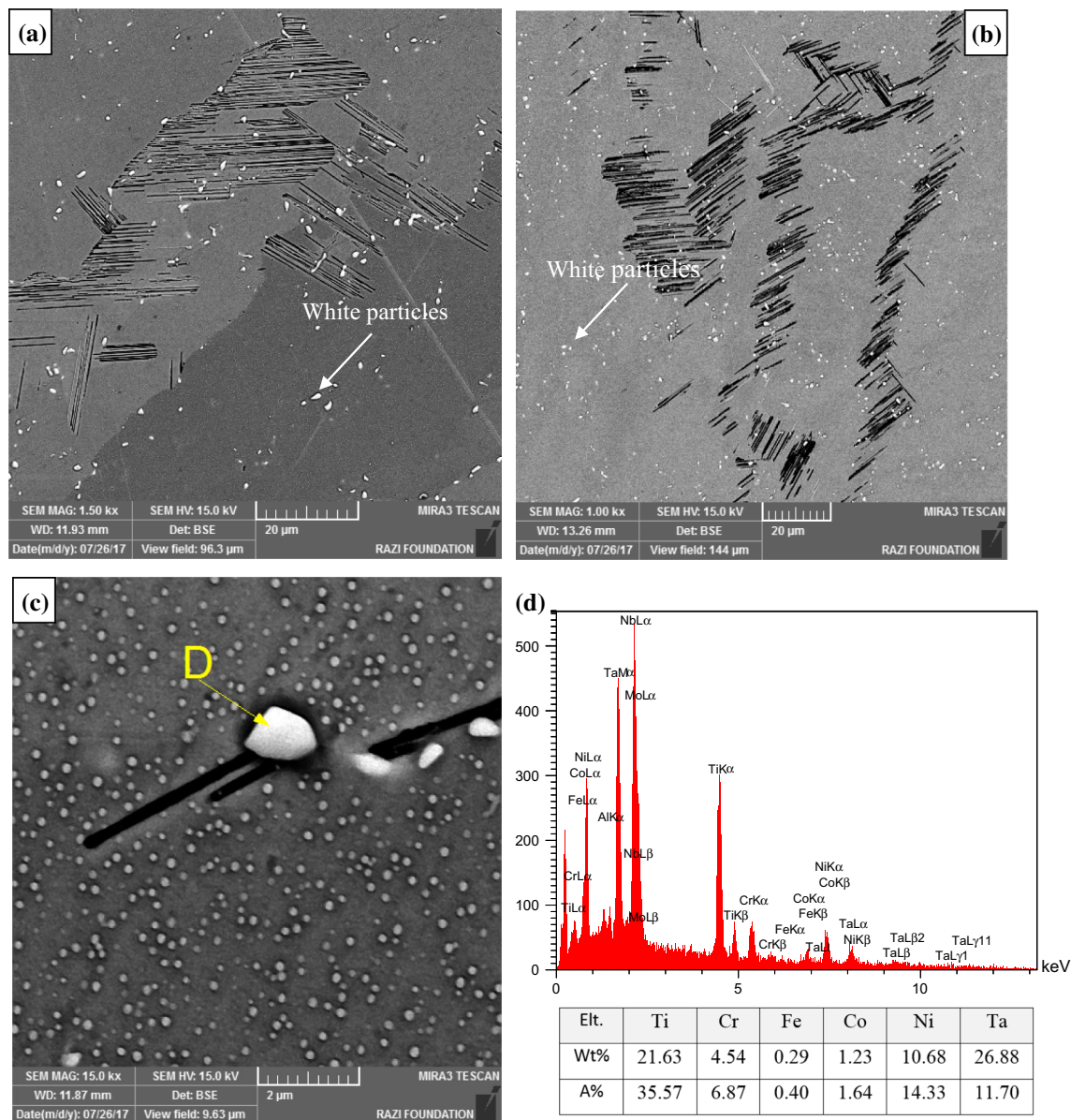


Fig. 6—FESEM micrographs of the WFZ of the specimen welded with (a) IN625 and (b) IN718 as filler metal, subjected to the 3-step PWHT cycle, indicating the precipitation of the δ , γ' particles and MC-carbide (c, d).

plate-like particles. The morphological evidence and EDS results prove that this is also an element of the δ phase. The circular precipitates in Figure 6(b) are γ' particles, with various diameters ranging from 30 to 100 nm. Reference 2 reported γ'' particles in the IN718 with a disc-shaped morphology, a thickness of about 10 nm, and a diameter of about 50 nm.^[2,24] In addition, discoidal γ'' phases with a diameter of 10 to 30 nm were reported in the IN625 alloy upon aging at 700 °C for 24 hours.^[25] The disc-shaped particles were not the same as those reported in references for alloys IN718 and IN625, in this study.

In order to study the microstructure of the specimens across the WFZ, optical and SEM images of the needle-shaped particles of the δ phase (Figures 2, 3, and 4) were investigated. Besides, electro-etching (deep

etching) was utilized to further examine the geometry of the plate-like particles of the δ phase (Figure 5). This morphology has been reported for the IN718.^[23,24] Different mechanisms have been proposed for nucleation and growth of the δ particles.^[23] Two precipitation mechanisms have been identified for the δ phase: (1) heterogeneous nucleation on the grain or along twin boundaries, and (2) the heterogeneous nucleation on the stacking faults in intragranular spaces within the γ'' phase^[21] (see Figure 3(a)). Precipitation of the δ phase in the IN625 and IN718 has been reported at various temperatures ranging within 750 °C to 950 °C.^[9] Given that the aging process was performed at temperatures falling within the above range for both the 3- and 4-step PWHT cycles (Table II), the formation of the δ phase was somewhat expected.

Figure 8 also demonstrates the XRD patterns acquired per the WFZ of the specimen welded with IN625 as filler metal. This specimen was subjected to the 4-step PWHT. Confirming the previous results (microstructural analysis of the WFZ), this pattern indicates the characteristic diffraction peaks corresponding to the δ , γ' , and γ'' phases. In the absence of the γ' and γ'' phases, the δ phase could be identified by comparing the integrated intensities along the XRD patterns, while it was not possible in the presence of the γ' and γ'' phases due to the overlap of the respective peaks along the XRD spectrum.^[27–29] The overlapping was evident at a diffraction angle (2θ) of about 42 deg (Figure 8).

Figure 9 presents the time-temperature transformation (TTT) diagrams for the WFZ and IN625, IN718 (outputs of the JMatPro Software). Table V presents the chemical composition of the WFZ for each filler metal. According to Figure 8, the γ' , γ'' , η , δ , and laves phases were expected in the WFZ. Laves phase is an intermetallic compound with the A_2B type structure, where $A = \text{Fe, Ni, Cr}$ and $B = \text{Nb, Mo, Si}$. This phase is the topologically close-packed (TCP) phases.^[1] According to the results of the microstructural studies, the presence of the γ' and δ phases was evident, while the η and laves phases were not observed. According to the significant percentage of Ti, Nb and Ta in the chemical

composition of the WFZ (Table V) and their roles in the formation of the η phase,^[3] it was expected that the η phase can be seen in the microstructures of the these regions. The reason for the absence of this phase in the microstructures may be the formation of MC-carbides during the solidification of the weld that reduces the Ti, Nb and Ta available to form the η phase later on. The formation of these carbides which are rich in Ti, Nb and Ta can be seen in Figure 6. Another explanation that why no η and laves phases were observed in WFZ-IN718, may be their very low amounts in WFZ. In other words, it that can be said that the number of cross-sections which are investigated in the present work are not high enough for observation of η and laves phases, and if more number of cross-sections can be investigated, then maybe these phases can be observed in the microstructure.

The chemical compositions of weld fusion zones are different in comparison with the chemical composition of alloys IN718 and IN625 (Tables I and V). Therefore, it can be expected that the TTT diagrams for weld fusion zones (Figures 9(a) and (b)) should be different in comparison with the TTT diagrams of alloys IN625 and IN718 (Figures 9(c), (d)). The comparisons between the TTT diagrams show that the phase which may form during the cooling (γ' , γ'' and δ phases, etc.) are the same for both filler metals and the fusion zones. Furthermore, it can be seen that initially γ' phases form, and subsequently, the γ'' , δ phases are formed according to the temperature and time parameters.

As mentioned, the difference in TTT diagrams is the order by which γ' , γ'' and δ form. According to the TTT diagrams of WFZs, first the γ' phase forms in the temperature range of 1000 °C to 1050 °C and then δ and laves phase form in the temperature range of 750 °C to 800 °C. However, according to the TTT diagrams of IN625 and IN718 alloys, first both γ' and γ'' phases start to form at temperatures around 800 °C for IN625 and 900 °C for IN718. In addition, it can be seen that δ phase will form at temperatures around 850 °C and 950 °C for IN625 and IN718, respectively. The differences observed in these diagrams can be attributed to the differences in the chemical compositions and the role of the constituent elements such as Nb, Al and Ti in the formation of γ' , γ'' and δ phases.

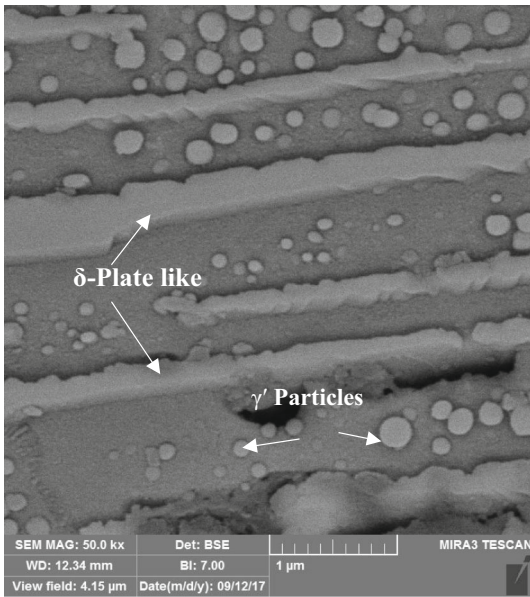


Fig. 7—FESEM micrographs of the WFZ of the specimen welded with IN718 as filler metal, subjected to the 4-step PWHT cycle, indicating the precipitation of the plate-shaped δ phase and γ' particles.

B. Phase Transformation and Formation of the δ Phase in the WFZ

Figure 10 shows the differential thermal analysis (DTA) curves of the WFZ obtained upon heating and cooling the specimen welded with IN625 as filler metal. According to this figure, the solidification stage occurred

Table IV. Quantitative Analysis of the Composition of the Plate-Like Particles (Fig. 7) Using the EDS Data

Element	Al	Ti	Cr	Co	Nb	Mo	Ta	Ni
Wt (Pct)	8.27	4.50	18.24	5.40	39.35	1.80	0.47	bal.
At. (Pct)	18.44	5.66	21.11	5.52	25.48	1.13	0.16	bal.

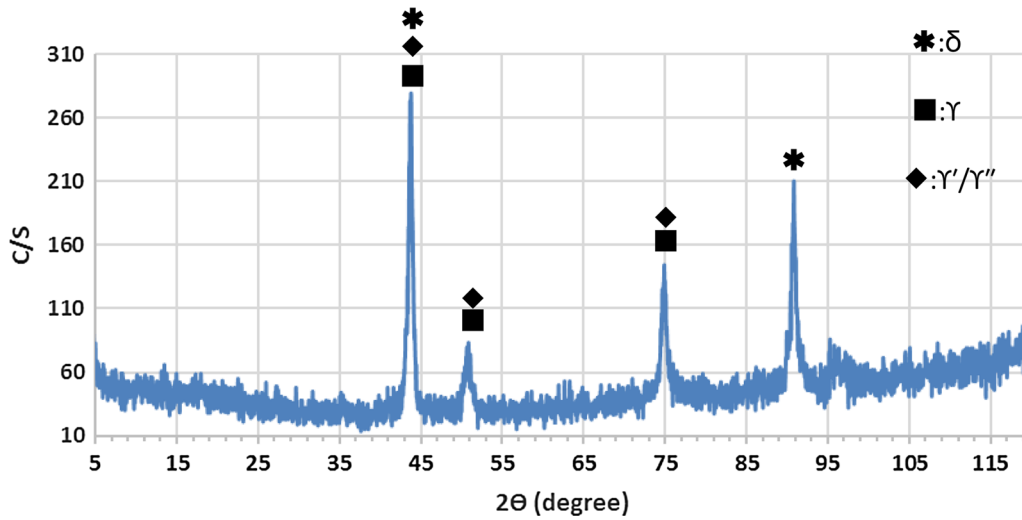


Fig. 8—The XRD patterns for the welds made with IN625 as filler metal and then subjected to the 4-step PWHT cycle showing the precipitation of the cellular δ phase particles and the γ'' (and γ') particles.

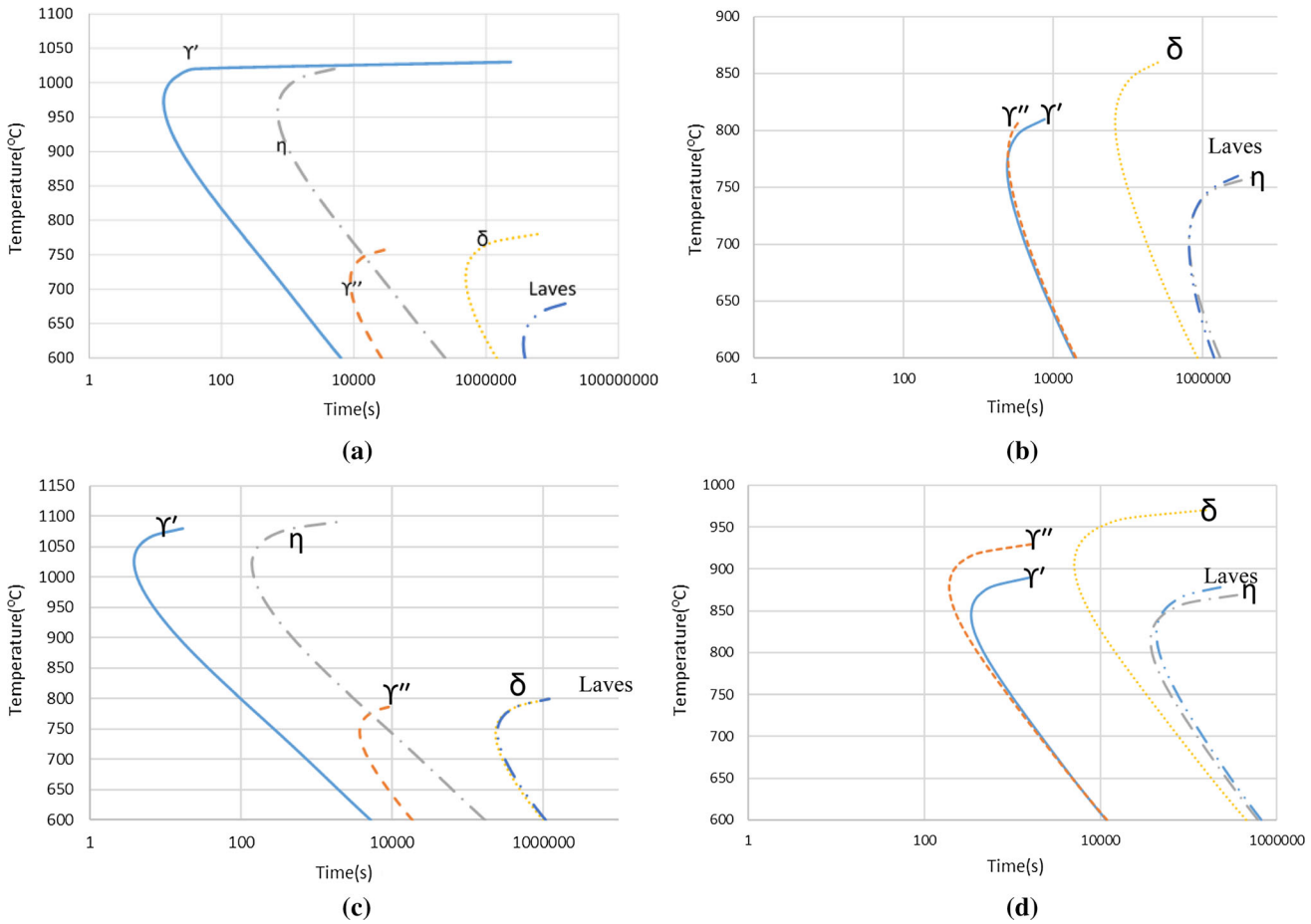


Fig. 9—The TTT diagrams of the WFZ of the specimens welded with (a) IN625 and (b) IN718 as filler metal and the TTT diagrams (c) IN625 and (d) IN718.

in the temperature range of 1370 °C to 1270 °C. Associated with the formation and dissolution of different phases, several endothermic and exothermic peaks were observed at 1275 °C, 1300 °C, 1325 °C, and

1350 °C. According to DTA and diff. DTA curves (Figure 10), when sample was cooled from 1400 °C, the exothermic peak was observed, which indicate the formation of the first nucleation of solid at a

temperature of about 1370 °C, can be observed. Therefore, the solidification starts with the following reaction at 1370 °C:



This reaction increases the concentration of the alloying elements (Nb, Ti, Ta, and Mo) in the remaining liquid (Figure 11). At 1325 °C, formation of the

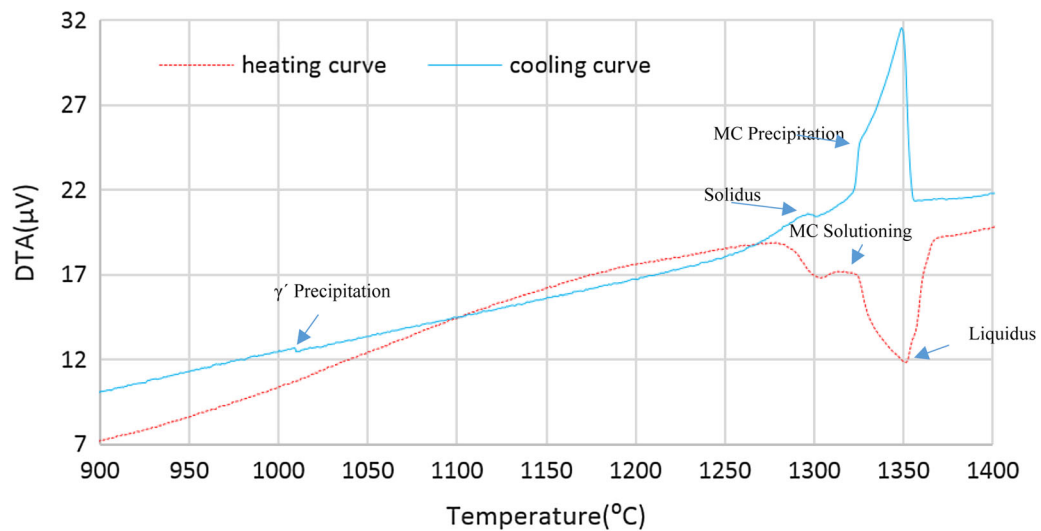
MC-carbide occurs via the following eutectic-like reaction:



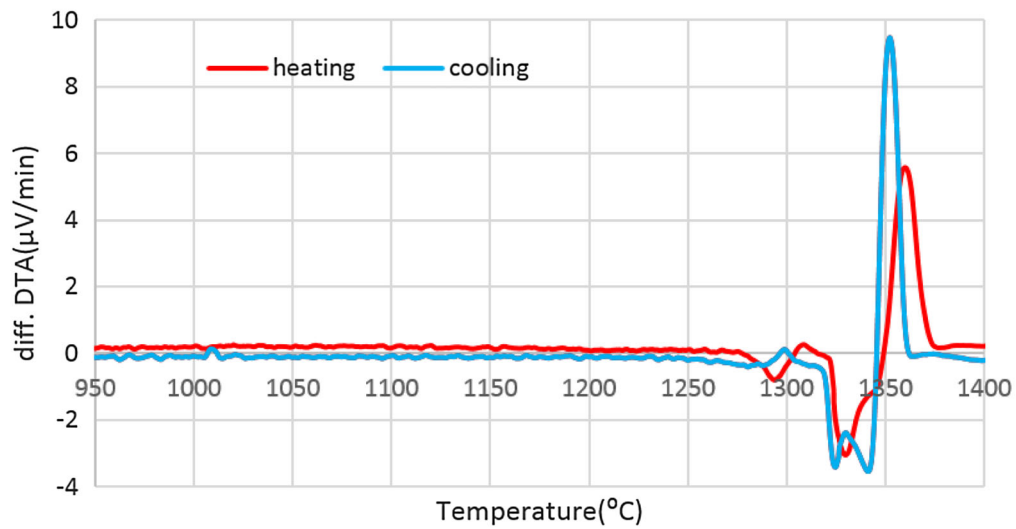
In order for the phase transformations to occur during the heating and cooling stages, the welded specimens were heated at different temperatures and then quenched. The corresponding results are presented later.

Table V. Chemical Composition of the WFZ, as per the EDS Data (Wt Pct)

Area/Element	Al	Ti	W	Ta	Cr	Fe	Nb	Mo	Co	Ni
WFZ-IN625	1.6	2.9	0	3.4	22.03	0.48	2.62	4.83	11.1	bal.
WFZ-IN718	1.73	3.43	1.82	1.03	21.69	5.17	2.49	1.63	12.92	bal.



(a)



(b)

Fig. 10—DTA & diff. DTA curves of the WFZ of the specimen welded with IN625 as filler metal, during the cooling and heating stages at a rate of 5 °C/min.

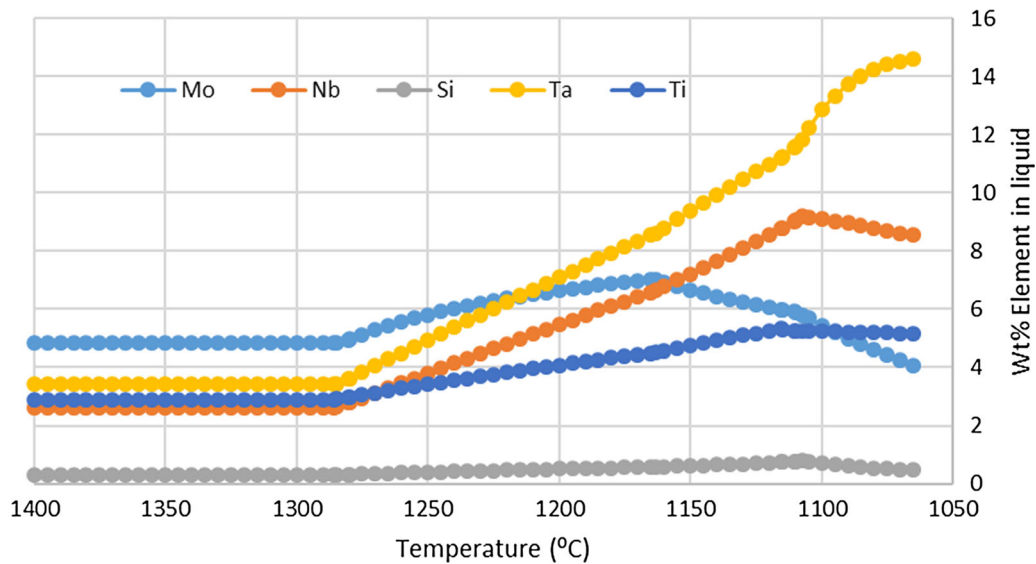


Fig. 11—The increased concentration of the alloying elements in the liquid phase after the solidification process (calculated by JMatpro Software).

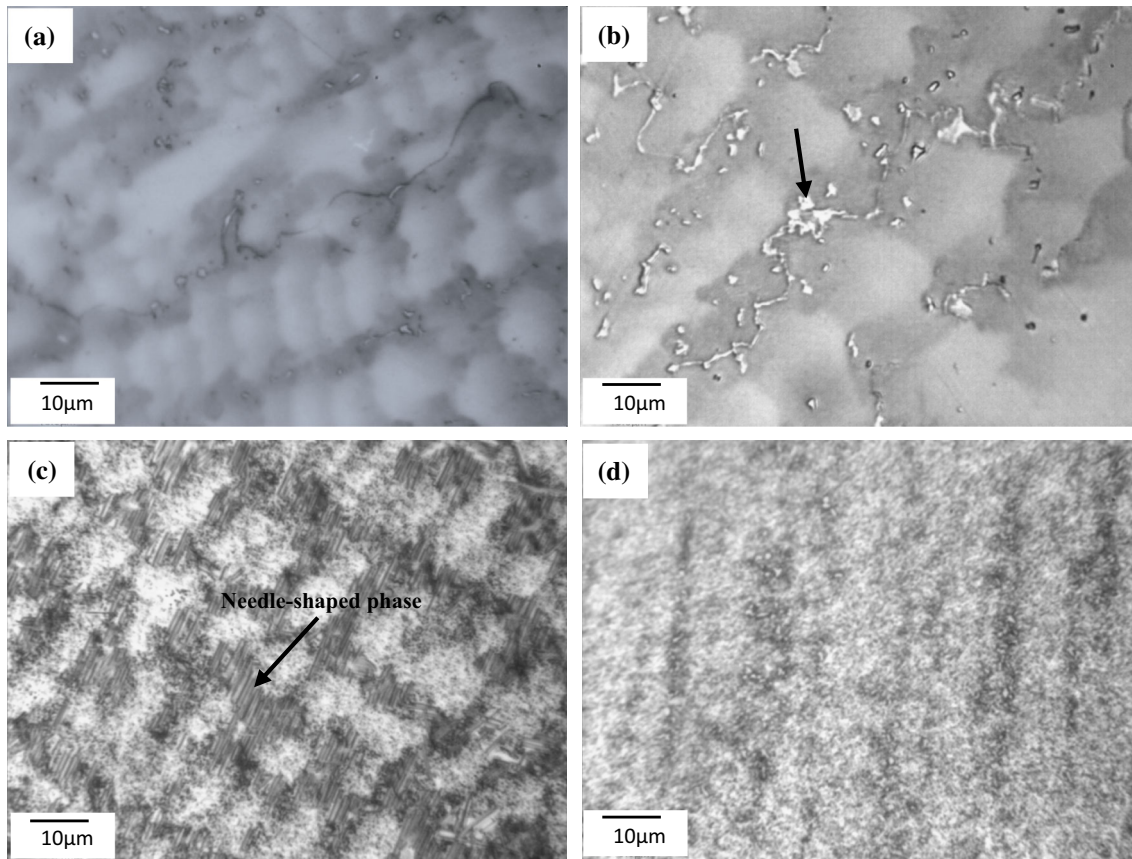


Fig. 12—Optical micrographs of the WFZ of the specimens subjected to PWHT at (a) 700 °C for 8 h, (b) 750 °C for 8 h, (c) 850 °C for 8 h, and (d) 1000 °C for 8 h. The specimens were welded with IN625 as filler metal.

Figure 12 shows the optical micrographs of the WFZ on the specimens were welded with IN625 as filler metal and subjected to PWHT at different temperatures.

Obviously, no microstructural variations were seen until the heating temperature reached 750 °C. At 850 °C, a phase transformation to a needle-shaped phase occurred

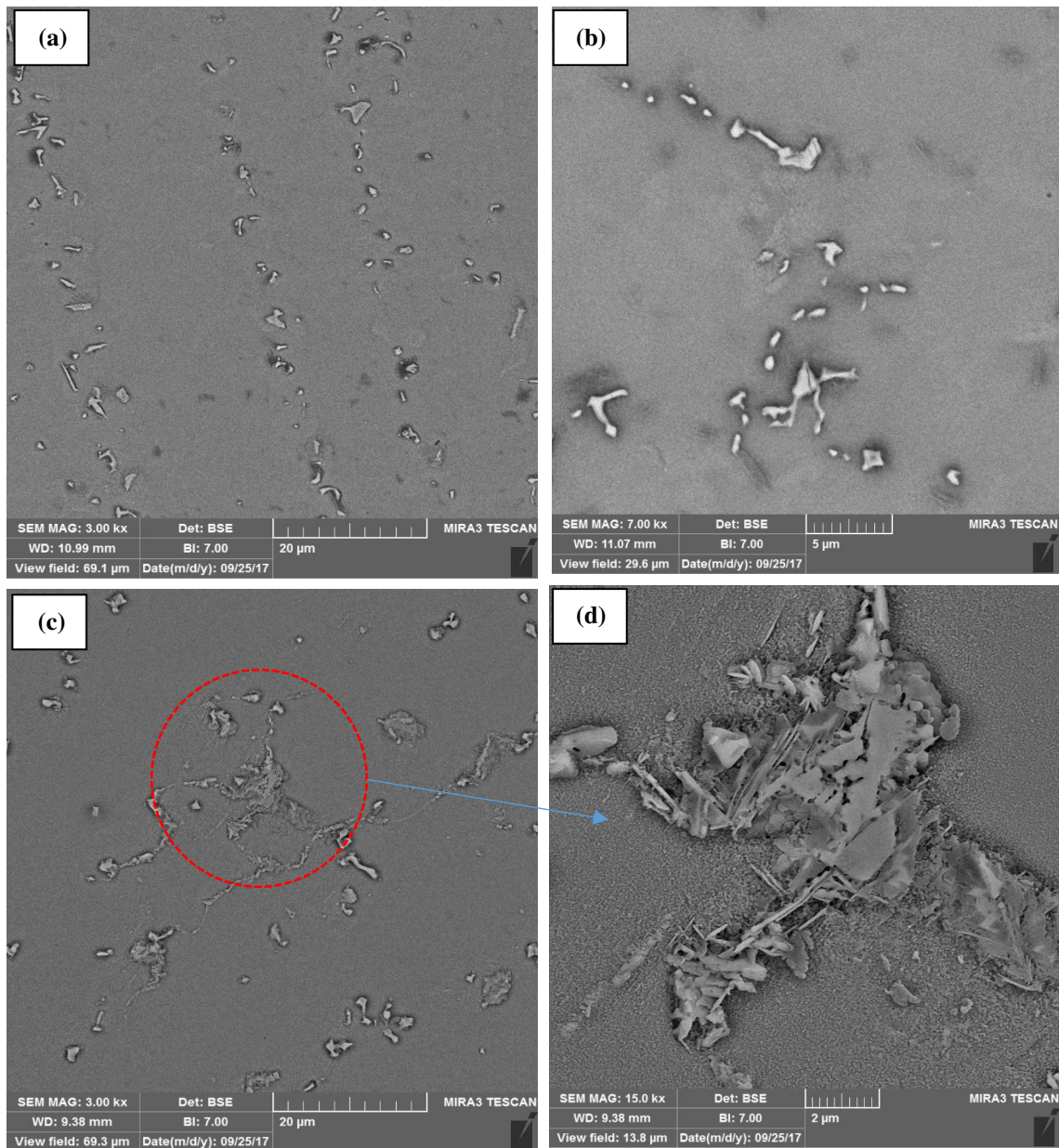


Fig. 13—SEM micrographs of the WFZ of the specimens subjected to PWHT at (a), (b) 700 °C for 8 h, and (c), (d) 750 °C for 8 h. The specimens were welded with IN625 filler metal.

in the inter-dendrite region (Figure 12(c)). At 1000 °C, the needle-shaped phase just disappeared (Figure 12(d)). As mentioned previously, the solute redistribution during the solidification of WFZ results in microsegregation across the core and inter-dendrite regions. The distribution of the alloying elements across the dendritic substructure in a Ni-based alloy is controlled by the equilibrium distribution coefficient (K) and the diffusivity of the element into the solid (D_s). Accordingly, the alloying elements with K values smaller than 1 tend to segregate toward the inter-cell or inter-dendrite arm boundary, while those with K values above 1 tend to segregate toward the core of cells or the dendrite arms. In general, elements with similar atomic radii to that of Ni (e.g., Fe, Cr, and Co) exhibit K values close to unity,

while such elements as Nb, Ti, Mo, Si, and C have less than 1 equilibrium distribution coefficients ($K < 1$), making them of high tendency toward segregation.^[1] The segregation of these elements was also predicted by JMatPro Software (Figure 11).

The formation of NbC and/or laves phases in the WFZ is due to the extensive separation of Nb and C in the solidification process.^[1] Indeed, Nb is required for the formation of the laves phase.^[1] On the other hand, both Al and Ti segregated in the solidification stage, thereby increasing the concentrations of Al and Ti in the liquid. This eventually enhances the Al and Ti concentrations to sufficient levels for terminating the solidification stage with a eutectic reaction involving the γ' -Ni₃Al ($L \rightarrow \gamma + \gamma'$) or η -Ni₃Ti phase ($L \rightarrow \gamma + \eta$).^[1]

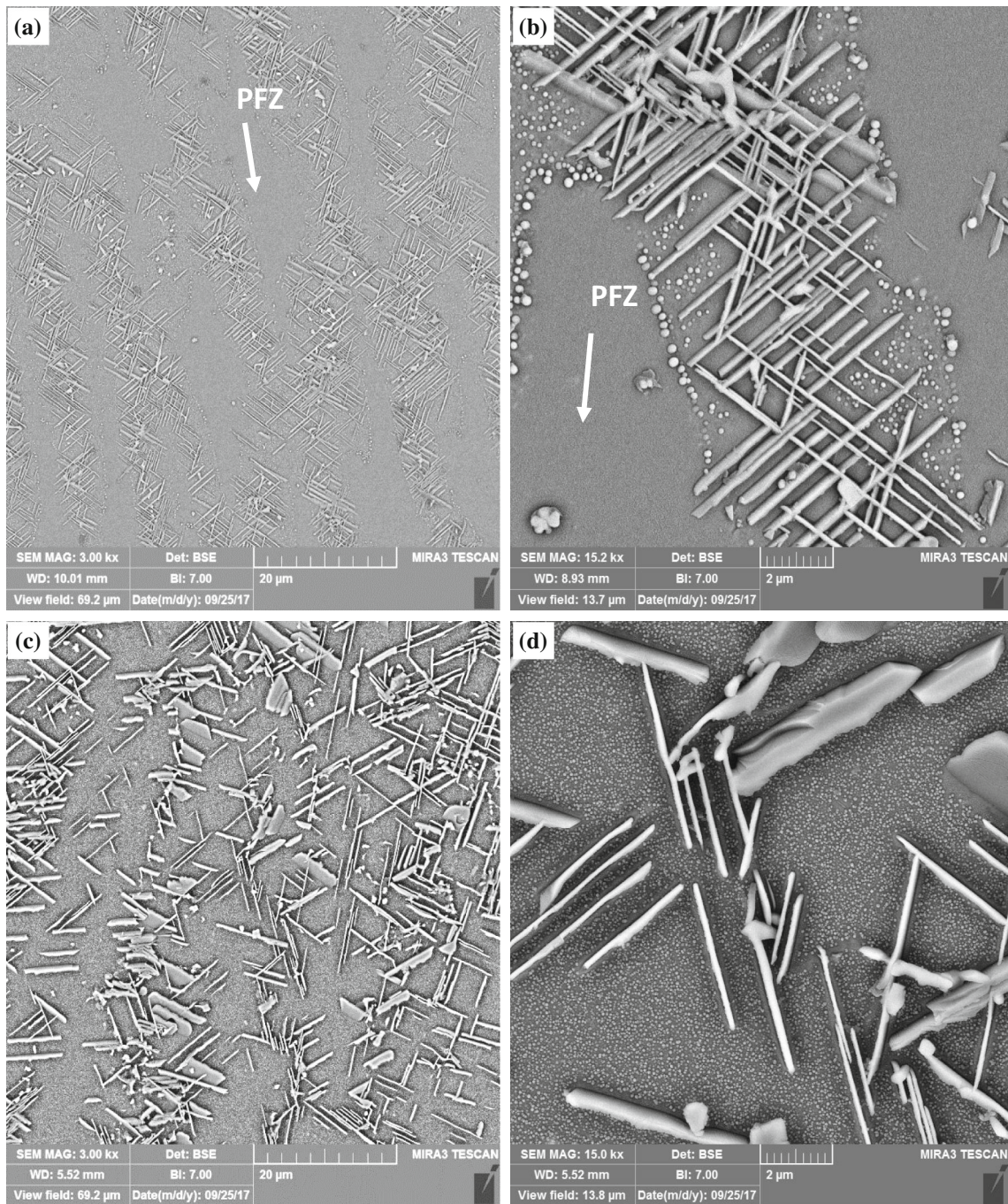
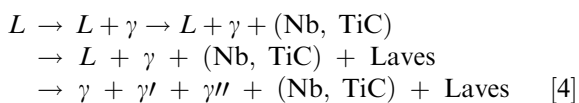


Fig. 14—SEM micrographs of the WFZ of the specimens subjected to PWHT at (a), (b) 850 °C for 8 h, and (c), (d) 900 °C for 8 h. The samples were welded with IN625 filler metal.

Therefore, one may propose the following sequence of phase transformations in the WFZ:



Figures 13, 14, and 15 show SEM images of the specimens subjected to PWHT at different temperatures. The samples were welded with IN625 filler metal. As

seen, at 700 °C, only the (Nb, Ti)C/laves phase was observed (Figures 13(a) and (b)). According to Figures 13(c) and (d), along with the (Nb, Ti)C/laves phase, some needle-shaped particles formed, indicating the start of the temperature window wherein this needle-shaped phase was formed. At this temperature, the γ'' phase was unstable and transformed to the δ phase ($\gamma''\text{-Ni}_3\text{Nb} \rightarrow \delta\text{-Ni}_3\text{Nb}$). Another researcher has reported this phase transformation at 700 °C.^[27] We believe that the higher temperature (750 °C) obtained in the present study is attributed to the shorter time of

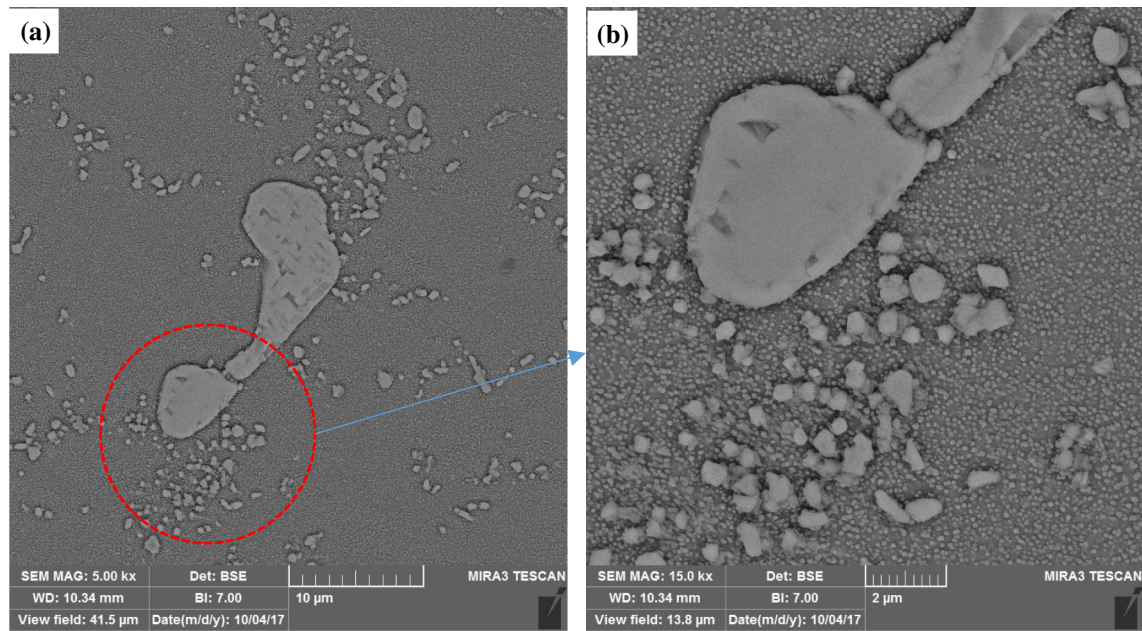
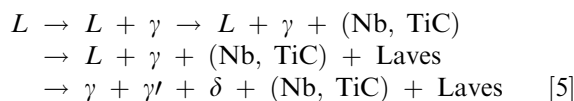


Fig. 15—SEM micrographs of the WFZ of the samples subjected to PWHT at (a), (b) 1000 °C for 8 h. The samples were welded with IN625 filler metal.

Table VI. Quantitative Analysis of the Composition of the WFZ on the Specimen Subjected to PWHT at 1000 °C for 8 Hours, as per the EDS Data

Element	Al	Ti	Cr	C	Co	Nb	Mo	Ta	Ni
Wt Pct	2.40	40.25	0.77	13.42	0.15	33.80	1.66	6.78	bal.
At. Pct	3.57	33.68	0.59	44.77	0.10	14.58	0.69	1.50	bal.

PWHT in our work (8 hours compared to 100 hours in Reference 27).



However, for AM IN625 alloy, the presence of γ'' precipitates has been reported at 870 °C (above the γ'' phase stability temperature).^[26] The enhanced concentration of Nb and Mo in the inter-dendrite region can affect the precipitation behavior of the δ and γ'' phases and their stability temperatures.^[27] With an increase in temperature, all inter-dendrite phases underwent a phase transformation into the needle-shaped phases (Figure 14).

The segregation and accumulation of the elements in the inter-dendrite region reduce the concentration of other elements (*e.g.*, Nb) in neighboring regions, thereby establishing a precipitate-free zone (PFZ) (Figures 14(a) and (b)). At 950 °C, the plate-like precipitates grew while the larger spherical precipitants were dissolved, leading to increased volume fraction of fine precipitants and destruction of the PFZ (Figures 14(c) and (d)).

No needle-like phase was observed at 1000 °C, suggesting that this temperature represents the dissolution temperature of this phase (Figure 15). A similar finding has been reported for the δ phase.^[1,29] Another work has ended up reporting a lower dissolution temperature of 950 °C for longer aging times (100 hours).^[30]

Table VI lists the results of the EDS analysis on the precipitate presented in Figure 15. As seen, this precipitate was rich in Ti and Nb, making it a MC-type carbide. In addition to the (Ti, Nb) C carbide phases, the γ'/γ'' particles were also observed in the samples (Figure 15(b)).

Figure 16 shows the FESEM images of the WFZ in the samples subjected to PWHT at 1293 °C, 1315 °C, and 1350 °C. The EDS analysis results (Table VII) confirmed the richness of these carbides in Nb and Ti, making them (Nb, Ti)C carbides. The figure further shows that the MC-carbide particles were decomposed at 1293 °C. Reference 29 has reported the decomposition of NbC-carbide in IN718 at 1264 °C.

C. Tensile Strength of Weldments

The tensile tests were performed in the temperature range of 25 °C (room temperature) to 900 °C. The samples were welded with IN625 filler metal and

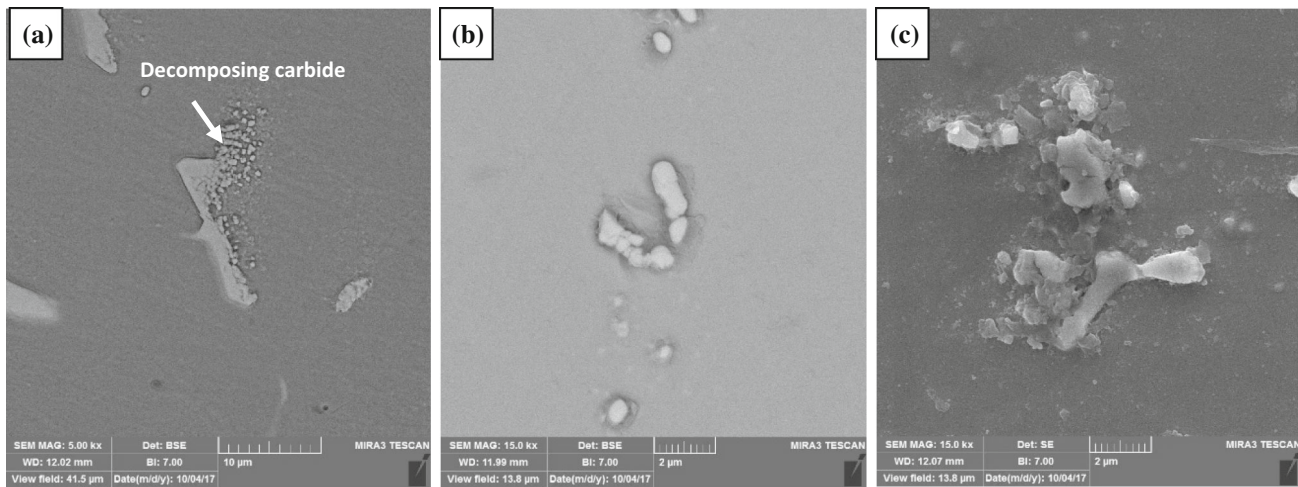


Fig. 16—FESEM micrographs of the WFZ of the specimens welded with IN625 as filler metal upon PWHT at (a) 1293 °C/WQ, (b) 1315 °C/WQ, and (c) 1360 °C/WQ, showing the decomposition of carbides. The samples were welded with IN625 filler metal.

Table VII. Quantitative Analysis of the Composition of the WFZ on the Specimen Subjected to PWHT at (a) 1293 °C/WQ and (b) 1350 °C/WQ, as per the EDS Data

	Element	Al	Ti	Cr	C	Co	Nb	Ta	Si	Ni
a	wt (pct)	5.12	12.48	9.79	12.37	2.65	42.00	1.78	3.69	bal.
	at. (pct)	7.65	10.51	7.59	41.54	1.81	18.23	0.40	5.30	bal.
b	wt (pct)	1.25	32.23	2.72	17.27	1.01	31.29	3.69	7.66	bal.
	at. (pct)	1.60	23.20	1.80	49.59	0.59	11.61	0.70	9.40	bal.

Table VIII. Mechanical Properties Obtained by the Tensile Tests at Room Temperature to 900 °C

Test Temperature (°C)	YS (MPa)	UTS (MPa)	El (Pct)
25	600	759	5
600	475	676	8.5
700	450	660	10
800	492	610	4
850	325	420	9
900	232	306	11

subjected to 4-step PWHT. The yield strength (YS), ultimate tensile stress (UTS), and elongation (EL) are presented in Table VIII and Figure 17. The YS values show an anomalous behavior as a function of the temperature. The yield strength show a decrease between 25 °C and 700 °C, followed by an increase (up to 800 °C) and then a rapid decrease at 900 °C. This bump in YS at high temperatures known as yield strength anomaly (YSA), has also been observed in other superalloy.^[31–34] It has been suggested that several mechanisms have been reported for it, especially in ordered alloys.^[35,36] Stress–strain curves from 25 °C up to 900 °C are shown in Figure 18. According to Figure 18, the tensile strength properties has decreased with increasing the temperature, but an increase at 800 °C and then a decrease up to 900 °C. The serrations

can be observed in the region of plastic deformation in the stress–strain curves at temperature between 600 °C and 900 °C. This type of plastic deformation instability in some metals is known as the Portevin–Le Chatelier (PLC) effect.^[37] The mechanism for the formation of serrations effect is dynamic strain aging (DSA) during plastic deformation. This phenomenon in turn affects the interaction of solute atoms (such as C, Mo and Cr) and mobile dislocations. The serrations type in stress–strain curves can vary with strain rates and temperature.^[37] At high strain rates and low temperature serrations of type A, at medium to high strain rate serrations of type B and at low strain rates and high temperatures serrations of type C can be observed. The serrations of type C are more regular.^[38,39] Type A serrations are termed locking serrations which can be associated with the nucleation of deformation bands in the specimen. This type of serrations fluctuates above the general flow curve. Type B serrations correspond to the hopping propagation of localized bands and considered locking serrations. These serrations fluctuate about the mean flow curve in very quick succession. When band propagation becomes limited, Type C serrations occur. Stress decrements associated with Type C serrations are often large and happen below the flow curve. Type C serrations are termed unlocking serrations. With decreasing the strain rate or increasing the temperature, the mode of serrations changes in order from Type A to Type B and then to Type C. While Type

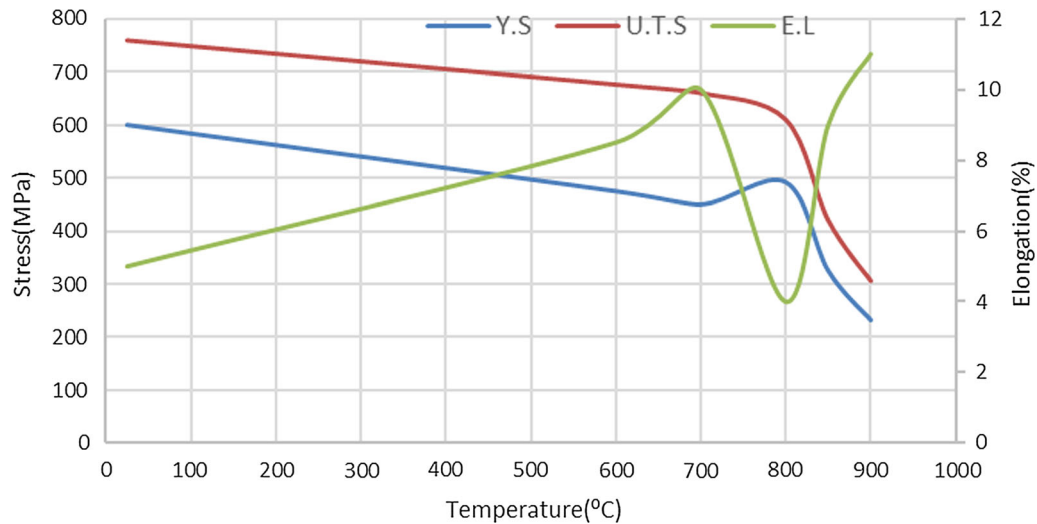


Fig. 17—Yield strength, ultimate strength, and elongation results of weldment as a function of the test temperature. The samples were welded with IN625 filler metal and subjected to 4-step PWHT.

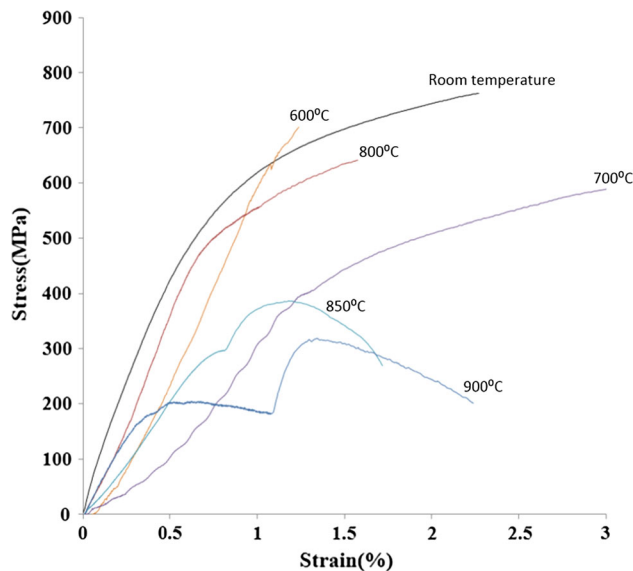


Fig. 18—Stress–strain curves of the weldments at different temperatures from 25 °C up to 900 °C. The samples were welded with IN625 filler metal and subjected to 4-step PWHT.

A is considered to be associated with aging of dislocations left behind the deformation front, Type B and C are related to the aging of moving dislocations within the deformation bands.^[39,40]

According to Figure 18, the A-type of serrations at temperature of 600 °C, the B-type serrations at temperatures of 800 °C, 850 °C and 900 °C of type 3 are observed. The serrations observed at 700 °C are C-type, which are formed due to the locking of dislocations by substitutional elements.^[40]

According to research done by the authors,^[16] the yield and ultimate strengths (YS, UTS) of the welding pool were compared to those of the standard IN939 alloy, showing 26 and 20 pct decrease, respectively, while the elongation (EL) of the welding pool was higher

by 89 pct. According to a study on the samples taken from 100,000-hours operated gas turbine blades under high temperature conditions, the presence of δ phases and extreme microstructural degradation, especially MC-carbides, changes in the size and morphology of γ' particles and reduction of the tensile properties are expected.^[40] On the other hand, considering the morphology of the δ phase on the mechanical properties,^[41] one can attribute part of this reduction to the plate-like δ phases.

Stress–strain curves of welded samples at 25 deg are shown in Figure 19. According to Figure 19, the ductility of the post-weld heat-treated sample is lower in comparison with as-welded sample. This could be due to the microstructural changes that occur during heat treatment according to the microstructural studies (Figures 3, 4, and 5). The percentage decrease in the elongation in the post-weld heat treatment sample is more than 50 pct compared to the as-welded samples. The effect of the δ phase in reducing of elongation has also been reported for IN625 and IN718.^[42,43]

IV. SUMMARY AND CONCLUSION

Examining TIG-welded IN939 weldments with IN625 and IN718 as filler metal, the following conclusions were drawn:

1. The microstructures of the weld fusion zone (WFZ) in both filler metals are consist of the matrix phase (γ) and secondary phases of γ' , δ and MC-carbides.
2. An increase in the concentrations of Nb and Ti in the inter-dendrite region of the WFZ contributes to the formation of (Nb, Ti)C carbide precipitates.
3. The post-weld heat treatments (PWHT) produce the δ and γ' phases in the WFZ.
4. The δ phase was observed in the WFZ upon PWHT at 750 °C for 8 hours. This phase was formed as plate-like $\sim 2 \mu\text{m}$ -thick precipitates at the grain

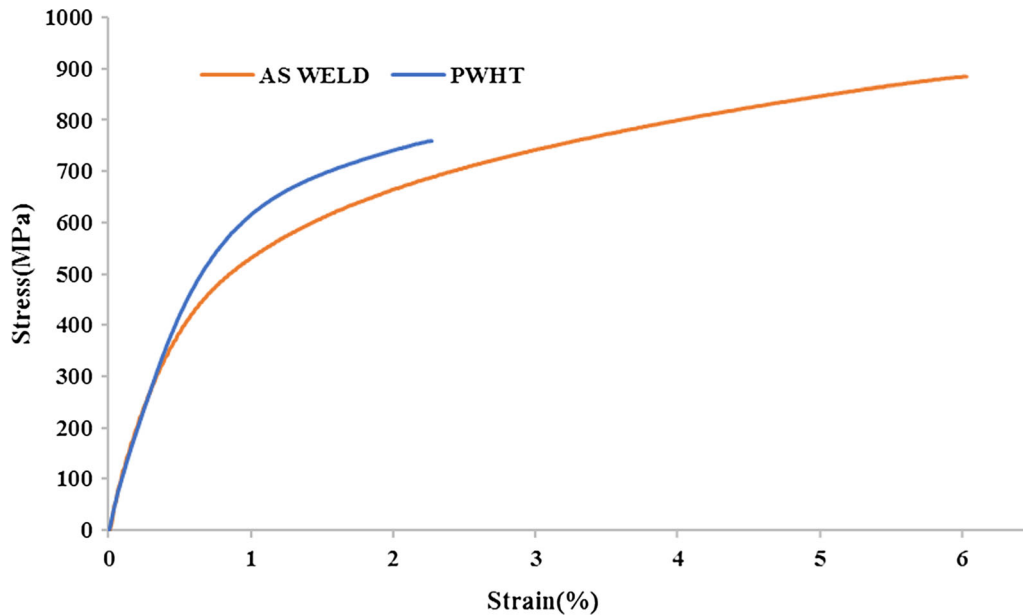


Fig. 19—Stress–strain curves of the weldments at 25 °C. The samples were welded with IN625 filler metal and tested at as-weld and post-weld heat-treated condition.

boundaries and inside the grains. At 1000 °C, this phase was dissolved in the matrix. Some precipitate-free zone (PFZs) were observed around the δ phase particles.

- The γ' particles with diameters ranging from 30 to 100 nm were observed in the WFZ.
- The solidification of WFZ was seen to occur at temperatures ranging between 1370 °C and 1270 °C.
- The MC-carbide started to decompose at temperatures above 1290 °C.
- Performing the standard PWHT on TIG-welded IN939 alloy made by IN625 and IN718 filler metals reduces the tensile properties of weldments at ambient temperature due to the formation of brittle δ phase.

ACKNOWLEDGMENT

The authors would like to acknowledge Niroo Research Institute (NRI) for providing the required research facilities.

CONFLICT OF INTEREST

The authors declare that they have no conflicts of interest.

REFERENCES

- J.C. Lippold, S.D. Kiser, and J.N. DuPont: *Welding Metallurgy and Weldability of Nickel-Base Alloys*, Wiley, New Jersey, 2011.
- R.C. Reed: *The Superalloys: Fundamentals and Applications*, Cambridge University Press, New York, 2008.
- T. Gibbons and R. Stickler: *Metallurgy, Properties and Performance, in High Temperature Alloys for Gas Turbines*, Springer, New York, 1982, pp. 369–93.
- C. Cutler and S. Shaw: *Strength of Metals and Alloys*, Elsevier, Amsterdam, 1980, pp. 1357–62.
- O. Ojo, N. Richards, and M. Chaturvedi: *Metall. Mater. Trans. A*, 2006, vol. 37A, pp. 421–33.
- O. Ojo, N. Richards, and M. Chaturvedi: *Scr. Mater.*, 2004, vol. 51, pp. 683–88.
- M. Strum, L. Summers, and J. Morris, Jr: *Weld. J.*, 1983, vol. 62, pp. 235s–42s.
- M.J. Donachie and S.J. Donachie: *Superalloys: A Technical Guide*, ASM International, Ohio, 2002.
- M. Sundararaman, P. Mukhopadhyay, and S. Banerjee: *Mater. Trans. A*, 1988, vol. 19, pp. 453–65.
- Y. Mei, Y. Liu, C. Liu, C. Li, L. Yu, Q. Guo, and H. Li: *Mater. Des.*, 2016, vol. 89, pp. 964–77.
- L.M. Suave, J. Cormier, P. Villechaise, A. Soula, Z. Hervier, D. Bertheau, and J. Laigo: *Metall. Mater. Trans. A*, 2014, vol. 45A, pp. 2963–82.
- E.A. Lass, M.R. Stoudt, M.E. Williams, L.E. Katz, T.Q. Levine, T.Q. Phan, T.H. Gnaeupel-Herold, and D.S. Ng: *Metall. Mater. Trans. A*, 2017, vol. 48A, pp. 5547–58.
- S. Manikandan, D. Sivakumar, and M. Kamaraj: *Symposium in the Recent Trends in the Plasticity and Phase Transformations*, Ruhr University, Bochum, 2015.
- Z.K. Low, T. Chaise, D. Bardel, S. Cazottes, P. Chaudet, M. Perez, and D. Nelias: *Acta Mater.*, 2018, vol. 156, pp. 31–42.
- G. Asala and O. Ojo: *Results Phys.*, 2016, vol. 6, pp. 196–98.
- H. Kazempour-Liasi, M. Tajally, and H. Abdollah-Pour: *Eng. Res. Express*, 2019, vol. 1, p. 025026.
- M. Abedini, M. Jahangiri, and P. Karimi: *Mater. High Temp.*, 2018, vol. 36 (1), pp. 19–26.
- Special metals: *INCONEL® alloy 718*, <http://www.specialmetals.com>.
- S. Kou: *Welding Metallurgy*, 2nd ed., Wiley, New Jersey, 2003, pp. 431–46.
- P. Quested and M. McLean: *The Metals Society*, University of Warwick, Coventry, 1983, pp. 586–91.
- C. Guoxin, Z. Maicang, D. Jianxin, Y. Zhihao, and Z. Lei: *Rare Met. Mater. Eng.*, 2014, vol. 43, pp. 103–08.
- M. Mathew, P. Parameswaran, and K.B.S. Rao: *Mater. Charact.*, 2008, vol. 59, pp. 508–13.
- S. Mahadevan, S. Nalawade, J.B. Singh, A. Verma, B. Paul, and K. Ramaswamy: *7th Int Symp Superalloys 718 Deriv*, vol. 737, 2010.
- M. Jouiad, E. Marin, R.S. Devarapalli, J. Cormier, F. Ravaux, C. Le Gall, and J.M. Franchet: *Mater. Des.*, 2016, vol. 102, pp. 284–96.

25. X. Xing, X. Di, and B. Wang: *J. Alloys Compds.*, 2014, vol. 593, pp. 110–16.
26. G. Marchese, M. Lorusso, S. Parizia, E. Bassini, J.W. Lee, F. Calignano, D. Manfredi, M. Terner, H.U.K. Hong, and D. Ugues: *Mater. Sci. Eng. A*, 2018, vol. 729, pp. 64–75.
27. S. Azadian, L.-Y. Wei, and R. Warren: *Mater. Charact.*, 2004, vol. 53, pp. 7–16.
28. E.A. Lass, M.R. Stoudt, M.B. Katz, and M.E. Williams: *Scr. Mater.*, 2018, vol. 154, pp. 83–86.
29. J. Ruan, N. Ueshima, and K. Oikawa: *J. Alloys Compds.*, 2018, vol. 737, pp. 83–91.
30. C.C. Silva, V.H.C. De Albuquerque, E.M. Mina, E.P. Moura, and J.M.R.S. Tavares: *Metall. Mater. Trans. A*, 2018, vol. 49, pp. 1653–73.
31. M.M. Oliveira, A.A. Couto, G.F.C. Almeida, D.A.P. Reis, N.B. Lima, and R. Baldan: *Metals*, 2019, vol. 9, p. 301.
32. K. Hrutkay and D. Kaoumi: *Mater. Sci. Eng. A*, 2014, vol. 599, pp. 196–203.
33. D. Kaoumi and K. Hrutkay: *J. Nucl. Mater.*, 2014, vol. 454, pp. 265–73.
34. F. Han, B.M. Zhou, H.F. Huang, B. Leng, Y.L. Lu, J.S. Dong, Z.J. Li, and X.T. Zhou: *Mater. Chem. Phys.*, 2016, vol. 182, pp. 22–31.
35. A.K. Roy and V. Marthandam: *Mater. Sci. Eng. A*, 2009, vol. 517, pp. 276–80.
36. P. Veysiere: *Mater. Sci. Eng. A*, 2001, vol. 309, pp. 44–48.
37. A. Cottrell: *Philos. Mag.*, 1953, vol. 44, pp. 829–32.
38. P. Rodriguez and S. Venkadesan: *Solid State Phenomena*, 1995, vol. 42, pp. 257–66.
39. P. Maj, J. Zdunek, M. Gizynski, J. Mizera, and K.J. Kurzydowski: *Mater. Sci. Eng. A*, 2014, vol. 619, pp. 158–64.
40. M. Jahangiri and M. Abedini: *Mater. Des.*, 2014, vol. 64, pp. 588–600.
41. W.D. Cao: *Superalloys*, 2005, vol. 718, pp. 166–77.
42. D. Liu, X. Zhang, X. Qin, and Y. Ding: *J. Mater. Sci. Technol.*, 2017, vol. 33, pp. 1610–17.
43. Y.L. Kuo, S. Horikawa, and K. Kakehi: *Mater. Des.*, 2017, vol. 116, pp. 411–18.

Publisher's Note Springer Nature remains neutral with regard to jurisdictional claims in published maps and institutional affiliations.